nature chemistry

Article

https://doi.org/10.1038/s41557-026-02078-w

Quantum interference between direct and indirect reaction paths in the photodissociation of HOD

Received: 16 October 2025

Accepted: 27 January 2026

Published online: 03 March 2026

Check for updates

Junyan Wang[1,12], Zijie Luo[2,3,12], Linsen Zhou[4], Xixi Hu[1,5,6], Zhenxing Li[7], Hua Guo[8], Shanyu Han[9,10] ✉, Daiqian Xie[1,6] ✉, Kaijun Yuan[2,6] ✉ & Xueming Yang[2,6,11]

The wave-like nature of quantum particles enables interference effects that can influence the outcomes of chemical reactions; however, most have been observed to occur from two spatially distinct reaction pathways, analogous to Young's double-slit experiment. Here we report detailed experiments on HOD photodissociation that reveal excitation-wavelength-dependent variations in the rotational state distribution of OD(X) product fragments. Full-dimensional quantum calculations reproduce the experimental observations semi-quantitatively, and our analysis attributes this behaviour to dynamical interferences between direct and indirect dissociation paths that both traverse the same conical intersection seam at collinear H–OD geometries, an interference analogous to 'single-slit diffraction' in optics. These observed dynamical signatures demonstrate that interference can manifest even within a single reaction pathway, suggesting a quantum mechanical means to control conical intersection-mediated nonadiabatic dynamics.

The wave nature of quantum particles underpins interference phenomena[1]. For example, when a matter wave traverses different paths, phase differences can produce constructive or destructive interference patterns in observable intensities, analogous to Young's double-slit experiment in optics[2]. Since the pioneer observation of electron double-slit interference[3], similar interference effects have been demonstrated in photoionization processes involving both atoms[4] and molecules[5–7]. Such wave-like behaviour can also influence measurable outcomes of a chemical reaction, manifesting as oscillatory patterns in product state or angular distributions[8–13].

Interference phenomena have been observed in several molecular systems. For instance, oscillatory differential cross-sections for NO–Ar collisions arise from interference between the N-end and O-end scattering paths[8]. Similarly, interference emerges between a direct and a roaming pathway in the H + HD reaction[10]. In the photodissociation of H_2O at 121.6 nm, oscillatory rotational state population distributions in the OH products were attributed to two different conical interactions (CIs) between the excited ($\tilde{B}$) and ground ($\tilde{X}$) states at linear H–OH and OH–H geometries[14]. In most of these cases, two spatially distinct pathways can be identified for the matter wave interference. A natural

[1]State Key Laboratory of Coordination Chemistry, Key Laboratory of Mesoscopic Chemistry of MOE, School of Chemistry and Chemical Engineering, Nanjing University, Nanjing, China. [2]State Key Laboratory of Chemical Reaction Dynamics and Dalian Coherent Light Source, Dalian Institute of Chemical Physics, Chinese Academy of Sciences, Dalian, China. [3]Marine Engineering College, Dalian Maritime University, Dalian, China. [4]Institute of Materials, China Academy of Engineering Physics, Mianyang, China. [5]Kuang Yaming Honors School, Institute for Brain Sciences, Nanjing University, Nanjing, China. [6]Hefei National Laboratory, Hefei, China. [7]Institute of Advanced Light Source Facilities, Shenzhen, China. [8]Department of Chemistry and Chemical Biology, Center for Computational Chemistry, University of New Mexico, Albuquerque, NM, USA. [9]International Center for Isotope Effects Research, State Key Laboratory of Critical Earth Material Cycling and Mineral Deposits, Nanjing University, Nanjing, China. [10]Frontiers Science Center for Critical Earth Material Cycling, School of Earth Sciences and Engineering, Nanjing University, Nanjing, China. [11]Department of Chemistry and Center for Advanced Light Source Research, College of Science, Southern University of Science and Technology, Shenzhen, China. [12]These authors contributed equally: Junyan Wang, Zijie Luo. ✉e-mail: shhan@nju.edu.cn; dqxie@nju.edu.cn; kjyuan@dicp.ac.cn

question arises: is it possible to observe interference within a single reaction pathway, analogous to optical single-slit diffraction? The verification of such interference has yet to be achieved experimentally or theoretically.

Nonadiabatic dynamics involving CIs provide an ideal setting in which to explore this question. CIs, where two or more electronic states become degenerate, are ubiquitous in chemistry and physics[15,16]. Their double-cone topologies serve as a chemical analogy of a funnel for nonadiabatic process, enabling rapid and efficient electronic relaxation in a wide range of systems—from elementary reactions[17,18] to biomolecular functions such as DNA photostability[19] and vision[20]. CIs are known to control many aspects of photochemical processes, including reaction pathways, excited-state relaxation, product yields and fluorescence lifetime[14,21–24]. Although these findings deepen our understanding of the topologies of CIs and of CI-induced nonadiabatic dynamics, the intrinsic dynamical features of the nonadiabatic path traversing a CI and their subtle influence on measurable outcomes are still not fully characterized.

The photochemistry of the water molecule offers a textbook example for understanding nonadiabatic dynamics involving CIs[25,26]. Absorption at wavelengths λ ~128 nm promotes the molecule to its second excited singlet ($\tilde{B}$) state. Some excited water molecules dissociate adiabatically on the $\tilde{B}$ state potential energy surface (PES) to produce electronically excited OH($A^2\Sigma^+$) fragments (along with an H atom), but the dominant photodissociation pathway for $\tilde{B}$ state molecules involves nonadiabatic coupling to the $\tilde{X}$ state PES via two CIs at linear H–OH and OH–H geometries. These nonadiabatic pathways result in formation of highly rotationally excited ground state OH($X^2\Pi$, $v = 0$) products[27–36]. Photodissociation via the higher-lying electronic $\tilde{D}$ state accessed by exciting near the Lyman-α wavelength ($\lambda = 121.6$ nm) is less well understood. The experimental evidence so far suggests fast conversion to the $\tilde{B}$ state PES via an avoided crossing (AVC) at bent geometries[36–38], followed by dissociation mechanisms similar to those for molecules excited directly to the $\tilde{B}$ state.

The present work reports a joint experimental–theoretical study of the photodissociation of partially deuterated water (HOD) molecules following excitation in the $\tilde{D}$–$\tilde{X}$ band at λ ~121 nm and demonstrates that the strongly wavelength-dependent OD(X) product rotational state population distributions are attributable to quantum interference between two distinct dissociation paths through a single CI funnel at linear H–OD geometries. One path involves direct traversal through the CI, while the other, henceforth termed the indirect path, involves transient trapping in the upper cone-shaped region of the CI before eventual transfer to the ground state. The phase difference between these two temporally distinct paths produces pronounced interference that manifests in the observed excitation-wavelength-dependent variations in the OD(X) product rotational distributions. Such peculiar signatures illustrate additional complexity in chemical reactions involving CI-induced nonadiabatic dynamics, which are expected to be general in many other systems.

Results and discussion

Experimental observation of highly excitation-wavelength-dependent OD(X) rotational state population distributions

The experiments were carried out using the H-atom Rydberg tagging time-of-flight (HRTOF) technique, combined with a tunable vacuum ultraviolet (VUV) source, as described in Methods (refs. 39–41). In brief, both the VUV photolysis beam and the 121.6 nm light for H atom fragment detection were generated using a tabletop VUV source from a difference frequency four-wave mixing scheme, involving two 212.556 nm photons and one photon at λ ~810–880 nm that overlapped in a Kr gas cell. A pulsed supersonic molecular beam of HOD was crossed by the VUV photolysis laser beam, and the H fragments were then detected by the HRTOF technique. The HOD sample was made by mixing H_2O and D_2O in a 1:5 volume ratio, which yielded an estimated H_2O/HOD ratio of ~1:9.5 (ref. 42) and ensured that the H atom signal arising from H_2O photolysis could be easily subtracted from the measured data. Knowing the distance travelled from the photodissociation region to the detector and the fragment masses, the recorded H atom TOF spectra can be converted into spectra of the total kinetic energy release (TKER) of the H + OD products.

Figure 1a,b shows typical TKER spectra recorded following photolysis of HOD at VUV wavelengths of 121.99 nm and 121.08 nm, respectively, with the polarization vector, $\boldsymbol{\varepsilon}_{\mathbf{phot}}$, aligned at the magic angle ($\theta = 54.7°$) to the detection axis, thereby ensuring that the spectra are insensitive to any product channel-dependent recoil anisotropy. The two spectra show obvious differences: the peak intensities at TKER values in the range 15,000–25,000 cm^{-1} are relatively much weaker in the spectrum obtained at 121.08 nm than at 121.99 nm. Additional TKER spectra obtained at 10 excitation wavelengths in the range $122.36 \geq \lambda \geq 120.86$ nm, with $\boldsymbol{\varepsilon}_{\mathbf{phot}}$ aligned parallel ($\theta = 0°$) and perpendicular ($\theta = 90°$) to the detection axis, are shown in Supplementary Fig. 1. Given that the total energy and linear momentum must be conserved in the photodissociation process, the internal energy (E_{int}) distribution of the OD fragments arising via H–OD bond fission can be determined from the TKER (E_{TKER}) distribution:

$$h\nu + E_{int}(\mathrm{HOD}) - D_0(\mathrm{H-OD}) = E_{TKER}(\mathrm{H+OD}) + E_{int}(\mathrm{OD}), \quad (1)$$

where h is the Planck constant, ν is the frequency of the excitation laser and D_0 is the dissociation energy. The rotational temperature of the water sample in the supersonic expansion was <10 K (ref. 32), that is, $E_{int}(\mathrm{HOD}) \approx 0$. Existing spectroscopic data allow most of the sharp features in Fig. 1 to be readily assigned to population of high rotational levels of OD(X) products in the $v = 0$ and 1 vibrational levels[43]. Best fits to the measured TKER distributions yielded the OD(X) rotational and vibrational state population distributions shown in Fig. 1c–f and Supplementary Figs. 2 and 3. These distributions all show high levels of product rotational excitation, reminiscent of that observed in the cases of H_2O and D_2O dissociation from the $\tilde{B}$ (or $\tilde{D}$) states[32,37,38], which can be attributed to the large angular torsion when the HOD molecule evolves from the bent Franck–Condon (FC) region towards the H–OD CI at linear geometries.

The key observation here is that the OD(X) rotational distribution varies dramatically with excitation energy. At $\lambda = 121.99$ nm, the dominant OD(X, $v = 0$) product exhibits a broad rotational distribution (spanning rotational levels with N ~30–55), with a minor narrow shoulder at N ~55–60. At $\lambda = 121.08$ nm, by contrast, the narrow high N component within the OD(X) product state distribution is dominant, while the broad (N ~30–55) component is relatively minor. Further, the OD(X, v) state distribution changes from regular to inverted upon switching between the two wavelengths; excitation at 121.08 nm yields an inverted vibrational distribution favouring OD(X) products with $v = 1$. Supplementary Figs. 2 and 3 show that the relative intensities of the broad and narrow components within the OD(X) rotational distribution are sensitively dependent upon the choice of excitation wavelength. At $\lambda = 120.86$ nm, for example, the two components make comparable contributions to the overall OD(X, $v = 0$) rotational state population.

Theoretical illustration of quantum interference via a single CI

To explore the dissociation mechanism of HOD photolysis at λ ~121 nm, full-dimensional quantum dynamics calculations were undertaken using a newly developed diabatic potential energy matrix (DPEM), as detailed in Methods. This DPEM includes the four lowest states of $^1A'$ symmetry (the $\tilde{X}/\tilde{B}/\tilde{D}/\tilde{E}'$ states) and a rigorous treatment of the nonadiabatic couplings between them, including five CIs and an AVC (Supplementary Figs. 5 and 6). Note that the first excited ($\tilde{A}$) state of water has $^1A''$ symmetry and thus is not included in the present

https://doi.org/10.1038/s41557-026-02078-w

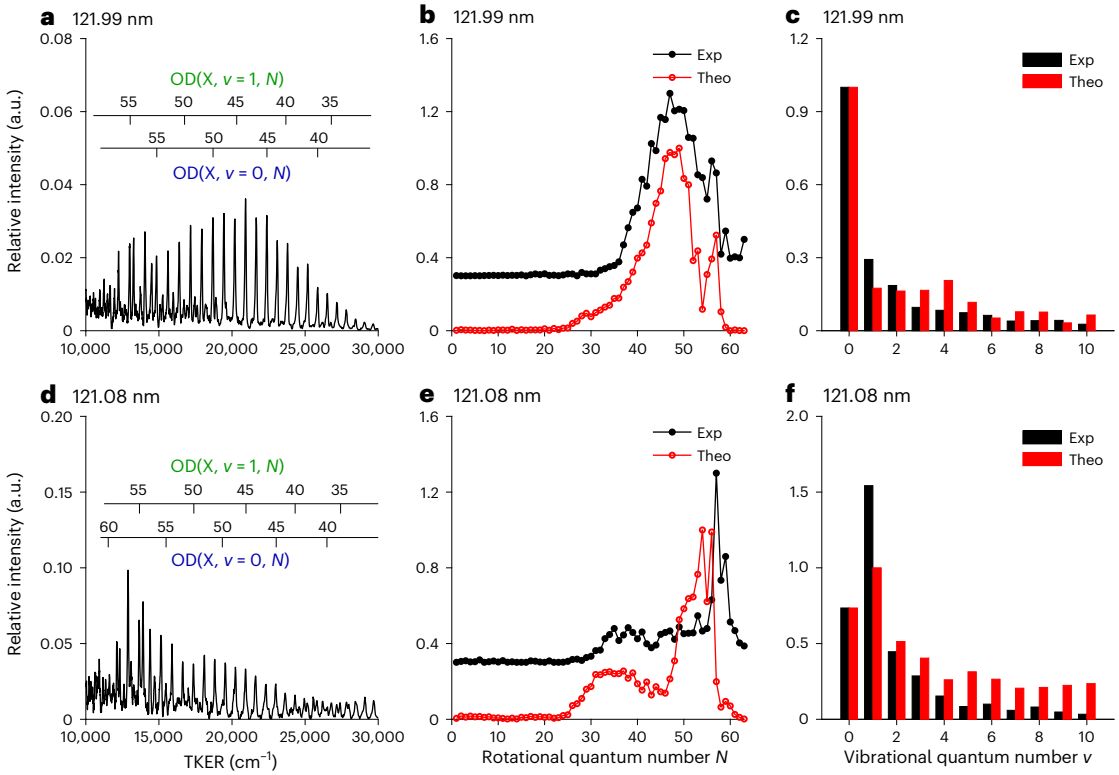

Fig. 1 | Comparison between experimental measurements and theoretical calculations. a,**d**, The TKER spectra from HOD photodissociation at $\lambda = 121.99$ nm (**a**) and 121.08 nm (**d**), with the detection axis aligned at 54.7° (magic angle) to ε_{phot}. Most of the sharp peaks are assigned to population of rotational states of OD(X, $v = 0$ and 1). The experimental (black) and theoretical (red) OD(X, $v = 0$) rotational state population distributions formed from HOD photodissociation at $\lambda = 121.99$ nm and 121.08 nm are shown in **b** and **e**, respectively, while **c** and **f** show the OD(X) vibrational state population distributions at these two wavelengths. The experimental results are labelled as Exp, while the theoretical's are labelled as Theo in panels **b**, **c**, **e** and **f**. The experimental rotational distributions in **b** and **e** have been offset vertically by 0.3 a.u. for display purposes.

calculations. This is a recognized omission at the present time (Supplementary Section 3). As Supplementary Fig. 7 shows, the H_2O absorption spectrum calculated using this new DPEM is in exceptionally good agreement with the available experimental data[44–46], successfully reproducing the $\tilde{B}-\tilde{X}$ band profile, the $\tilde{D}-\tilde{X}$ band centre and the absolute absorption cross-sections. The experimental absorption data for HOD is more limited, restricted to excitation wavelengths >126.5 nm, but, again, the present DPEM enables impressive reproduction of the available HOD($\tilde{B}-\tilde{X}$) band profile.

The $\tilde{B}$ and $\tilde{A}$ states of water are degenerate at linear geometries, and Renner–Teller coupling is another recognized nonadiabatic route for photoexcited HOD($\tilde{B}$) molecules to dissociate to H + OD(X) products. However, its contribution is relatively minor at low parent rotational temperatures[35] and not noticeably excitation wavelength dependent, as illustrated by the results of wavepacket calculations[47] (Supplementary Figs. 8 and 9) following excitation at various wavelengths within the $\tilde{B}-\tilde{X}$ continuum.

Figure 1 compares the experimentally OD(X) rovibrational state population distributions determined at $\lambda = 121.99$ nm and 121.08 nm with those predicted by the present calculations. Similar comparisons for data measured at eight other wavelengths are shown in Supplementary Figs. 2 and 3. The agreement between experiment and theory is semi-quantitative in all cases, both with respect to the actual distributions, and their excitation wavelength dependence. Good agreement is also obtained for more detailed spatial information, namely the recoil anisotropy parameters (Supplementary Fig. 4).

After a rapid nonadiabatic transition from the initially prepared $\tilde{D}$ state to the $\tilde{B}$ state in the FC region (Supplementary Figs. 10 and 11), molecules are drawn towards the deep potential wells at linear geometries on the $\tilde{B}$ state PES associated with the H–OD and OD–H CIs. Numerical simulations illustrate that artificially blocking the CI at linear OD–H configurations has negligible impact on the OD(X) distributions (Supplementary Fig. 12), consistent with the minimal wavefunction amplitude in this region (Fig. 4). This implies that the experimentally observed OD(X) rotational distributions largely derive from dynamical paths traversing just the H–OD CI, rather than from two dissimilar CI (H–OD and OD–H linear geometries) pathways as reported earlier in H_2O photodissociation around 121.6 nm (refs. 14,48).

To aid mechanistic interpretation of the nonadiabatic dynamics, we also resorted to semiclassical trajectory surface hopping calculations[49]. Similar to wavepacket evolution, trajectories after the $\tilde{D}\rightarrow\tilde{B}$ transfer are funnelled into the upper conical adiabat of the H–OD CI by the strong O–H bond extension and angular forces prevailing in the FC region of the $\tilde{B}$ state PES. A vast majority (~91%) dissociate on the $\tilde{X}$ state PES after hopping near the H–OD CI. Further analysis of the dissociation trajectories initiated by excitation at λ ~121.08 nm reveals two characteristic architypes that lead to different sets of rotationally excited OD(X) fragments. As shown by the example trajectories in Fig. 2, 'direct' dissociations transition to the $\tilde{X}$ state by a single pass through the CI, while 'indirect' dissociations are characterized by transient trapping in the upper cone-shaped adiabat before eventually jumping to the $\tilde{X}$ state PES. This distinction originates from differences in how the trajectories approach the CI: direct trajectories tend to enter closer to the CI seam, increasing the probability of immediate hopping, whereas indirect trajectories approach the CI at larger displacements, leading to delayed transitions (Supplementary Fig. 13). These two classes of trajectory have been identified previously in the study of OH(A) products from H_2O photolysis and in spectral simulations of warm water[50–52].

https://doi.org/10.1038/s41557-026-02078-w

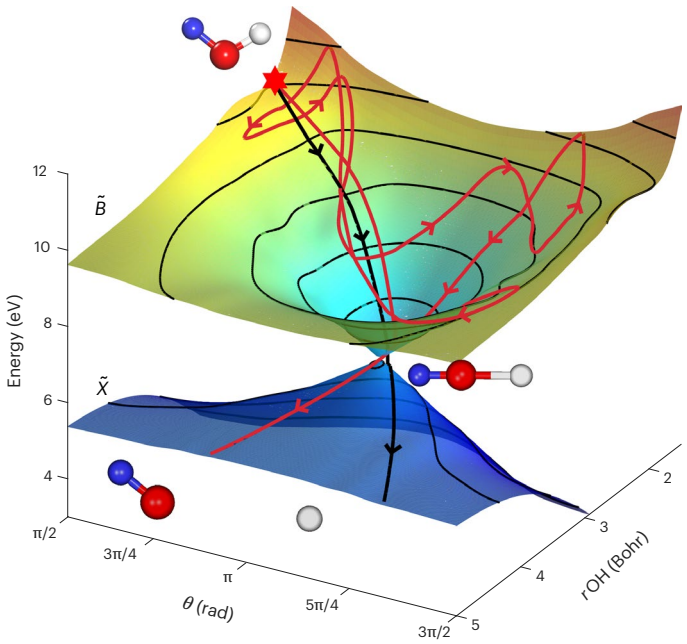

Fig. 2 | Schematic view of the H–OD CI between the $\tilde{B}$ and $\tilde{X}$ state PESs at linear geometries, together with illustrative 'direct' and 'indirect' trajectories. A three-dimensional view of the $\tilde{B}$ and $\tilde{X}$ state PESs around the linear H–OD CI. The direct path (black curve with arrows) represents trajectories transitioning to the $\tilde{X}$ state via a direct pass through the CI, while the indirect path (red curve with arrows) is characterized by transient trapping in the upper cone-shaped adiabat before eventually jumping to the $\tilde{X}$ state. Atoms are colour-coded as H (grey), D (blue) and O (red). The red star marks the start position for each trajectory on the $\tilde{B}$ state PES.

The large difference in trajectory lifetimes of the two paths (the average lifetimes on the $\tilde{B}$ state PES are 9.5 fs versus 46 fs), as shown in Supplementary Fig. 13b, motivated us to disentangle their contributions by monitoring product distributions accumulated over time in the wavepacket calculations. This can be achieved by calculating the accumulated time-dependent product quantum state distributions, as shown in Fig. 3a,b. At λ ~ 121.99 nm, the OD(X) products with N in the range 30–50 accumulate monotonically, whereas, at λ ~121.08 nm, products with N = 25–40 initially increase but subsequently decline, suggesting destructive interference from the delayed contributions.

In the quantum dynamics calculations, all the product information is determined by a complex-valued quantity known as the T-matrix[53]. The state-resolved cross-section is then directly proportional to the square of the modulus of this quantity. The temporal evolution allows us to decompose the T-matrix into direct and indirect contributions, $T = T^{\text{direct}} + T^{\text{indirect}}$. As such, the final cross-section could be expressed as

$$\sigma_{v,N} = |T^{\text{direct}}_{v,N}|^2 + |T^{\text{indirect}}_{v,N}|^2 + 2|T^{\text{direct}}_{v,N}||T^{\text{indirect}}_{v,N}| \cos \Delta, \qquad (2)$$

where the interference term depends on the relative phase (Δ) between the two paths as well as the relative strength of the corresponding T-matrix elements. Although the division between direct and indirect paths based on lifetime is somewhat arbitrary, the respective contributions from each path to the overall cross-section can be guided by the reflection principle[25,54], that is, the direct dynamics generally yield smooth, excitation energy-insensitive, state-resolved cross-sections. Figure 3c,d shows decomposed cross-sections for forming OD(X, v = 0, N) fragments via the direct and indirect paths, and their interference term, when exciting at λ ~121.99 nm and ~121.08 nm, respectively. In both cases, the two paths are predicted to make comparable contributions to the total OD(X, v = 0) product distribution, but to interfere very differently—weakly at λ ~121.99 nm, but destructively at λ ~121.08 nm. In the latter case, the destructive interference results in a marked suppression of population in the N ~25–40 range. Supplementary Figs. 14 and 15 show similar decompositions of the OD(X, v = 0, N) and OD(X, v = 1, N) distributions from the direct and indirect paths and the associated interference term at the other excitation wavelengths investigated. As expected, the product rotational state distributions from the direct path are relatively insensitive to excitation wavelength. Those arising via the indirect path, by contrast, exhibit more oscillatory structure and notable variations with excitation wavelength. The interference term also varies dramatically with excitation energy, flipping from net negative to positive and then back to negative again across the $\tilde{D}$–$\tilde{X}$ band contour (Supplementary Figs. 16–21).

Further insight into the nature of the interference is obtained by examining the scattering wavefunctions in the $\tilde{B}$ and $\tilde{X}$ states at the two representative excitation energies (Fig. 4). The scattering wavefunctions are solutions to the Schrödinger equation for scattering states, and the square of their modulus gives the probability distribution over all possible paths in coordinate space. To focus on a specific product vibrational state, the total wavefunction has been projected onto the OD(X, v = 0) manifold, by integrating over the internuclear distance. At both wavelengths, the $\tilde{B}$ state wavefunction emanating from the $\tilde{D}$/$\tilde{B}$ AVC is accelerated towards the linear H–OD CI owing to the strong torque exerted by the PES. Some of the flux undergoes nonadiabatic transition to the $\tilde{X}$ state near this CI and proceeds to produce H + OD(X) products, while the remainder continues on the $\tilde{B}$ state PES to form H + OD(A) products. As Fig. 4 shows, the outgoing wavefunction on the $\tilde{X}$ state PES at the two excitation wavelengths shows distinct differences. At λ ~121.99 nm, the $\tilde{X}$ state wavefunction

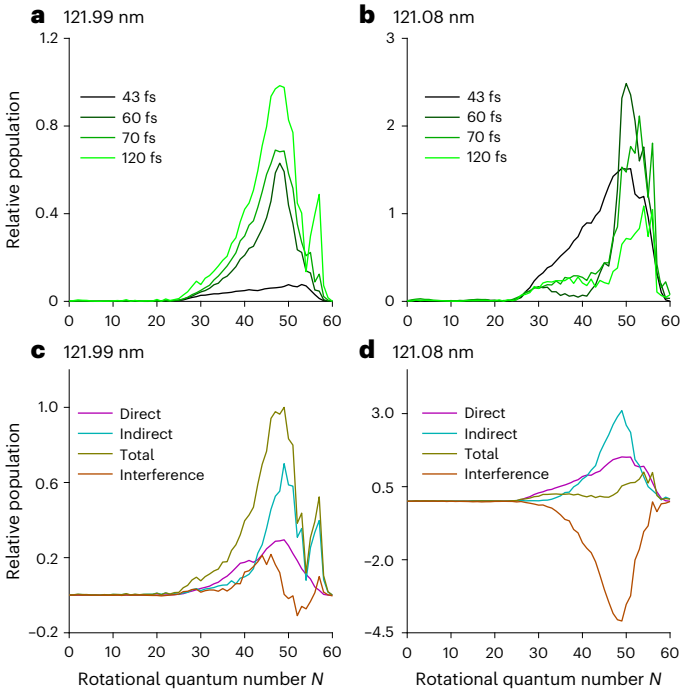

Fig. 3 | Time-dependent rotational state distributions and the decomposed distributions. a,**b**, The rotational state distributions of OD(X, v = 0) fragments as a function of propagation time from wavepacket calculations at excitation wavelengths of λ ~121.99 nm (**a**) and λ ~121.08 nm (**b**). Here the propagation times given in the insets in the upper panels are the times from launching the wavepacket (at t = 0) over which products can accumulate in the asymptotic (analysis) region. **c**,**d**, The decomposed OD(X, v = 0, N) product distributions arising via the two paths and their interference term at excitation wavelengths of λ ~121.99 nm (**c**) and λ ~121.08 nm (**d**).

https://doi.org/10.1038/s41557-026-02078-w

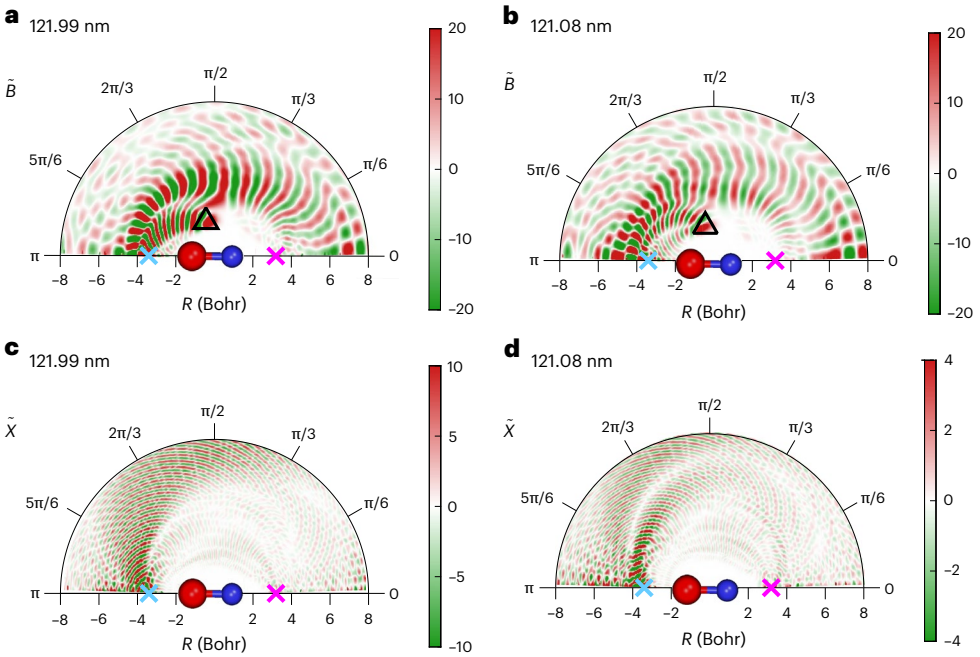

Fig. 4 | Scattering wavefunctions at λ ~121.99 nm and 121.08 nm. a–**d**, The wavefunction on the $\tilde{B}$ state PES at λ ~ 121.99 nm (**a**) and 121.08 nm (**b**). The wavefunction on $\tilde{X}$ state PES at λ ~ 121.99 nm (**c**) and 121.08 nm (**d**). Wavefunction amplitudes are scaled for display purposes. The triangle symbols in **a** and **b** indicate the point of AVC between the $\tilde{D}/\tilde{B}$ state PESs at which the wavefunctions access the $\tilde{B}$ state. The wavefunction shown in **d** displays two intense arcs separated by a region in which the amplitude is strongly attenuated, representing clear evidence for destructive interference. The cyan and magenta crosses denote the H–OD and OD–H CIs, the red and blue balls represent the O and D atoms, and the black triangle marks the initial position of the H atom on the $\tilde{B}$ state PES, respectively.

evolving from the H–OD CI appears as a single broad arc with alternating positive and negative nodes, characteristic of plane-wave motion. At λ ~121.08 nm, however, the $\tilde{X}$ state wavefunction comprises two arcs, separated by a region in which the amplitude is strongly attenuated, which represents clear evidence for destructive interference. Time-resolved plots depicting the evolution of the $\tilde{X}$ state wavefunction (Supplementary Fig. 18) provide further demonstration of a dynamic interference pattern arising from phase cancellation between temporally separated contributions in the case of λ ~121.08 nm excitation.

Conclusion

In summary, the present work attributes the striking excitation-wavelength-dependent OD(X) product rotational state population distributions observed in the photodissociation of $\tilde{D}$ state HOD molecules to quantum interferences between distinct dynamical paths mediated by a single CI between the $\tilde{B}$ and $\tilde{X}$ state PESs at linear H–OD geometries. One, direct, path features molecules that undergo single-pass nonadiabatic transitions near the CI. In the other, indirect, path, molecules are transiently trapped in the potential well associated with the CI on the $\tilde{B}$ state PES before nonadiabatic coupling to the $\tilde{X}$ state and eventual dissociation. Interestingly, these two paths spatially belong to the same reaction pathway, but can be distinguished temporally. The reported dynamics calculations reproduce the experimental observations semi-quantitatively, thereby providing strong support for the proposed mechanism. This presents an example that quantum interference can emerge within a single reaction pathway, an analogue of single-slit diffraction in optics. These findings suggest that such phenomena might be a more general and previously under-appreciated feature of CI-mediated molecular dynamics. They also suggest another potential route to quantum control of chemical reactions involving passage through a CI. For instance, techniques such as optical cavities[55] and phase-controlled laser pulses[56] allow the manipulation of the characteristic of CI and the relative phase between the paths via the CI, which could lead to control of nonadiabatic dynamics of competing reaction pathways and product state populations. However, a key challenge would be a priori knowledge acquisition of the nonadiabatic dynamics at the CI needed for precise control, particularly in complex systems.

Online content

Any methods, additional references, Nature Portfolio reporting summaries, source data, extended data, supplementary information, acknowledgements, peer review information; details of author contributions and competing interests; and statements of data and code availability are available at https://doi.org/10.1038/s41557-026-02078-w.

References

1. De Broglie, L. Waves and quanta. *Nature* **112**, 540–540 (1923).
2. Hecht, E. *Optics* (Pearson, 2012).
3. Jönsson, C. Elektroneninterferenzen an mehreren künstlich hergestellten Feinspalten. *Zeitschrift für Physik* **161**, 454–474 (1961).
4. Pursehouse, J., Murray, A. J., Wätzel, J. & Berakdar, J. Dynamic double-slit experiment in a single atom. *Phys. Rev. Lett.* **122**, 053204 (2019).
5. Akoury, D. et al. The simplest double slit: interference and entanglement in double photoionization of H_2. *Science* **318**, 949–952 (2007).
6. Kunitski, M. et al. Double-slit photoelectron interference in strong-field ionization of the neon dimer. *Nat. Commun.* **10**, 1 (2019).
7. Canton, S. E. et al. Direct observation of Young's double-slit interferences in vibrationally resolved photoionization of diatomic molecules. *Proc. Natl Acad. Sci. USA* **108**, 7302–7306 (2011).
8. Eyles, C. J. et al. Interference structures in the differential cross-sections for inelastic scattering of NO by Ar. *Nat. Chem.* **3**, 597–602 (2011).

9. Zhou, H., Perreault, W. E., Mukherjee, N. & Zare, R. N. Quantum mechanical double slit for molecular scattering. *Science* **374**, 960–964 (2021).
10. Xie, Y. et al. Quantum interference in H + HD → H_2 + D between direct abstraction and roaming insertion pathways. *Science* **368**, 767–771 (2020).
11. Jambrina, P. G. et al. Quantum interference between H + D_2 quasiclassical reaction mechanisms. *Nat. Chem.* **7**, 661–667 (2015).
12. Reilly, C. S. et al. Quantum interference observed in state-resolved molecule-surface scattering. *Science* **387**, 962–967 (2025).
13. Liu, Y. et al. Quantum interference in atom-exchange reactions. *Science* **384**, 1117–1121 (2024).
14. Dixon, R. N. et al. Chemical "double slits": dynamical interference of photodissociation pathways in water. *Science* **285**, 1249–1253 (1999).
15. Domcke, W., Koppel, H. & Yarkony, D. R. *Conical Intersections: Electronic Structure, Dynamics & Spectroscopy* (World Scientific, 2004).
16. Yarkony, D. R. Diabolical conical intersections. *Rev. Mod. Phys.* **68**, 985–1013 (1996).
17. Zhang, Y., Yuan, K., Yu, S. & Yang, X. Highly rotationally excited CH_3 from methane photodissociation through conical intersection pathway. *J. Phys. Chem. Lett.* **1**, 475–479 (2010).
18. Yuan, D. et al. Observation of the geometric phase effect in the H + HD → H_2 + D reaction below the conical intersection. *Nat. Commun.* **11**, 3640 (2020).
19. Schultz, T. et al. Efficient deactivation of a model base pair via excited-state hydrogen transfer. *Science* **306**, 1765–1768 (2004).
20. Polli, D. et al. Conical intersection dynamics of the primary photoisomerization event in vision. *Nature* **467**, 440–443 (2010).
21. Ashfold, M. N. R. et al. The role of πσ* excited states in the photodissociation of heteroaromatic molecules. *Science* **312**, 1637–1640 (2006).
22. Lim, J. S. & Kim, S. K. Experimental probing of conical intersection dynamics in the photodissociation of thioanisole. *Nat. Chem.* **2**, 627–632 (2010).
23. Ashfold, M. N. R. et al. Exploring nuclear motion through conical intersections in the UV photodissociation of phenols and thiophenol. *Proc. Natl Acad. Sci. USA* **105**, 12701–12706 (2008).
24. Sage, A. G. et al. nσ* and πσ* excited states in aryl halide photochemistry: a comprehensive study of the UV photodissociation dynamics of iodobenzene. *Phys. Chem. Chem. Phys.* **13**, 8075–8093 (2011).
25. Schinke, R. *Photodissociation Dynamics: Spectroscopy and Fragmentation of Small Polyatomic Molecules* (Cambridge Univ. Press, 1993).
26. Yuan, K., Dixon, R. N. & Yang, X. Photochemistry of the water molecule: adiabatic versus nonadiabatic dynamics. *Acc. Chem. Res.* **44**, 369–378 (2011).
27. van Harrevelt, R. & van Hemert, M. C. Photodissociation of water. I. Electronic structure calculations for the excited states. *J. Chem. Phys.* **112**, 5777–5786 (2000).
28. van Harrevelt, R. & van Hemert, M. C. Photodissociation of water. II. Wave packet calculations for the photofragmentation of H_2O and D_2O in the *B* band. *J. Chem. Phys.* **112**, 5787–5808 (2000).
29. Fillion, J. H. et al. Photodissociation of H_2O and D_2O in $\tilde{B}$, $\tilde{C}$, and $\tilde{D}$ (134-119 nm). Comparison between experiment and ab initio calculations. *J. Phys. Chem. A* **105**, 11414–11424 (2001).
30. Dixon, R. N. Λ-doublet and spin-doublet population-distributions in the products of photofragmentation via coupled electronic channels—H_2O(B-tilde $^1A_1$)→H+OH($X^2\Pi$). *J. Chem. Phys.* **102**, 301–309 (1995).
31. Mordaunt, D. H., Ashfold, M. N. R. & Dixon, R. N. Dissociation dynamics of H_2O(D_2O) following photoexcitation at the Lyman-alpha wavelength (121.6 nm). *J. Chem. Phys.* **100**, 7360–7375 (1994).
32. Harich, S. A. et al. Photodissociation of H_2O at 121.6 nm: a state-to-state dynamical picture. *J. Chem. Phys.* **113**, 10073–10090 (2000).
33. Yi, W., Park, J. & Lee, J. Photodissociation dynamics of water at Lyman alpha (121.6 nm). *Chem. Phys. Lett.* **439**, 46–49 (2007).
34. Jiang, B., Xie, D. & Guo, H. State-to-state photodissociation dynamics of triatomic molecules: H_2O in the *B* band. *J. Chem. Phys.* **136**, 034302 (2012).
35. Hwang, D. W., Yang, X. & Yang, X. The vibrational distribution of the OH product from H_2O photodissociation at 157 nm: discrepancies between theory and experiment. *J. Chem. Phys.* **110**, 4119–4122 (1999).
36. Chang, Y. et al. Hydroxyl super rotors from vacuum ultraviolet photodissociation of water. *Nat. Commun.* **10**, 1250 (2019).
37. Chang, Y. et al. Photodissociation dynamics of H_2O and D_2O via the $\tilde{D}$ ($^1A_1$) electronic state. *Phys. Chem. Chem. Phys.* **22**, 4379–4386 (2020).
38. Yuan, K. et al. Two-photon photodissociation dynamics of H_2O via the $\tilde{D}$ electronic state. *J. Chem. Phys.* **131**, 074301 (2009).
39. Harich, S. A., Yang, Y. & Yang, X. Extremely rotationally excited OH from water (HOD) photodissociation through conical intersection. *Phys. Rev. Lett.* **87**, 253201 (2001).
40. Harich, S. A. et al. Single rotational product propensity in the photodissociation of HOD. *Phys. Rev. Lett.* **87**, 263001 (2001).
41. Yuan, K. et al. Nonadiabatic dissociation dynamics in H_2O: competition between rotationally and nonrotationally mediated pathways. *Proc. Natl Acad. Sci. USA* **105**, 19148–19153 (2008).
42. Luo, Z. et al. Strong isotope effect in the VUV photodissociation of HOD: a possible origin of D/H isotope heterogeneity in the solar nebula. *Sci. Adv.* **7**, eabg7775 (2021).
43. Coxon, J. A. Optimum molecular constants and term values for the $X^2\Pi(v\leq5)$ and $A^2\Sigma^+(v\leq3)$ states of OH. *Can. J. Phys.* **58**, 933–949 (1980).
44. Bodi, A. et al. VUV absorption spectra of water and nitrous oxide by a double-duty differentially pumped gas filter. *J. Synchrotron Radiat.* **31**, 1257–1263 (2024).
45. Mota, R. et al. Water VUV electronic state spectroscopy by synchrotron radiation. *Chem. Phys. Lett.* **416**, 152–159 (2005).
46. Cheng, B. et al. Quantitative spectroscopic and theoretical study of the optical absorption spectra of H_2O, HOD, and D_2O in the 125–145 nm region. *J. Chem. Phys.* **120**, 224–229 (2004).
47. Zhou, L. & Xie, D. Full-dimensional quantum dynamics of vibrational mediated photodissociation of HOD in its *B* band. *J. Phys. Chem. A* **119**, 12062–12072 (2015).
48. Zhou, L., Xie, D. & Guo, H. Signatures of non-adiabatic dynamics in the fine-structure state distributions of the OH(*X*/*A*) products in the *B* band photodissociation of H_2O. *J. Chem. Phys.* **142**, 124317–124326 (2015).
49. Tully, J. C. Molecular dynamics with electronic transition. *J. Chem. Phys.* **93**, 1061–1071 (1990).
50. van Harrevelt, R. & van Hemert, M. C. Photodissociation of warm water: ab initio calculations of the room-temperature absorption spectrum. *Chem. Phys. Lett.* **370**, 706–711 (2003).
51. Segev, E. & Shapiro, M. Three-dimensional quantum dynamics of H_2O and HOD photo-dissociation. *J. Chem. Phys.* **77**, 5604–5623 (1982).
52. Weide, K., Kuhl, K. & Schinke, R. Unstable periodic orbits, recurrences, and diffuse vibrational structures in the photodissociation of water near 128 nm. *J. Chem. Phys.* **91**, 3999–4008 (1989).
53. Balint-Kurti, G. & Shapiro, M. Quantum theory of molecular photodissociation. *Adv. Chem. Phys.* **60**, 403–450 (1985).
54. Schinke, R. & Engel, V. The rotational reflection principle in photodissociation dynamics. *Faraday Discuss. Chem. Soc.* **82**, 111–124 (1986).

55. Gu, B. & Mukamel, S. Manipulating nonadiabatic conical intersection dynamics by optical cavities. *Chem. Sci.* **11**, 1290–1298 (2020).
56. Liu, N. et al. Optical control of crossing the conical intersection in β-carotene. *J. Phys. Chem. Lett.* **14**, 9215–9221 (2023).

Methods

Experimental methods

The VUV photodissociation dynamics of HOD were studied using the HRTOF technique, coupled with a tunable VUV source, which has been described previously[41]. The H fragments were excited from the ground state to a high Rydberg state via a two-step excitation: from $n = 1$ to $n = 2$ and from $n = 2$ to n ~45. The first excitation step was made by absorbing a 121.6 nm photon generated by difference four wave mixing (DFWM) of 212.556 nm and 845 nm photons in a gas cell filled with 25% Kr in Ar. The tunable VUV photolysis source for the HOD photodissociation between 120.86 nm and 122.36 nm was also generated by DFWM using the same 212.556 nm light as for the H-atom Rydberg tagging and another tunable source operating at wavelengths ~850 nm. Since 121.6 nm also generates H atom signals from HOD/H_2O photodissociation, background subtraction was achieved by alternating the photolysis laser on and off.

The HOD sample was made by mixing H_2O and D_2O. The HRTOF measurements of the H atom products from the mixed sample will have contributions from H_2O photolysis. To suppress such background signal, H_2O and D_2O were mixed with the volume ratio of 1:5, which produced a mixture with an H_2O/HOD ratio of ~1:9.5 (ref. 42). The HOD molecular beam was generated by expanding a sample of 3% HOD in Ar. The pulsed valve was adjusted with great care to ensure that very few water clusters were present in the HOD/Ar beam. The Rydberg-tagged H atoms were detected by a Z-stack microchannel plate detector with a grounded fine mesh in front of the detector. The signals were then recorded using a multi-channel scaler system. The energy resolution achieved ($\Delta E_{TKER}/E_{TKER}$ ~0.3% at E_{TKER} = ~10,000 cm^{-1}) allows population in different rotational states of the OD(X) products to be distinguished.

Four-state coupled DPEM

HOD excitation at wavelengths λ ~122 nm corresponds to the $\tilde{D} \leftarrow \tilde{X}$ excitation. To model the nonadiabatic dynamics, a four-state coupled DPEM was constructed for the four lowest electronic states of $^1A'$ symmetry: the $\tilde{X}$, $\tilde{B}$, $\tilde{D}$ and $\tilde{E}'$ states. This DPEM includes five conical intersections (CIs) and one AVC, as illustrated in Supplementary Figs. 5 and 6 (for the case of H_2O). At the FC region for C_{2v} geometries, both the $\tilde{B}$ and $\tilde{D}$ states belong to the A_1 irreducible representation (irrep) and their interaction leads to the well-known AVC owing to the strong mixing of the $1b_1 \rightarrow 3p_x/3a_1 \rightarrow 3s$ excitations[27]. At small bond angles (~78°), the state of $^1B_2$ symmetry crosses the two $^1A_1$ states, forming the $\tilde{E}'/\tilde{D}$ and $\tilde{D}/\tilde{B}$ CIs. At large bond angles (~130°), the $^1B_2$ state crosses the third $^1A_1$ state, giving rise to another lower energy $\tilde{E}'/\tilde{D}$ CI[57,58]. The various bending potential energy curves (C_{2v} geometry) shown in Supplementary Fig. 5a illustrate the AVC and the three aforementioned CIs, while Supplementary Fig. 5b,c shows cuts through the diabatic $\tilde{B}$ and $\tilde{X}$ state potentials upon extending just one O–H bond with ∠HOH = 180° and 0°, respectively. These regions of degeneracy (CIs) between the $\tilde{B}$ and $\tilde{X}$ state potentials at linear geometries are further illustrated in Supplementary Fig. 6.

As shown previously[59–63], the symmetry operators commute with the Hamiltonian; thus, symmetry adaptation is both advantageous and necessary for the evolution of the nuclear wave function. In the diabatization framework, we enforced the complete nuclear permutation-inversion (CNPI) symmetry of H_2O, which belongs to the G_4 group (isomorphic to C_{2v}). The four diabatic states are thus labelled as $1A_1$ (V_{11}), $2A_1$ (V_{22}), $3A_1$ (V_{33}) and $1B_2$ (V_{44}), based on their CNPI irreps. In this framework, diagonal elements of the DPEM, representing diabatic potentials, always belong to the totally symmetric irrep. However, off-diagonal elements, representing nonadiabatic couplings, could belong to a symmetric or anti-symmetric irrep, depending on the interacting states. For instance, the off-diagonal coupling between $2A_1$ ($\tilde{B}$) and $3A_1$ ($\tilde{D}$) states (involved in the AVC) must be symmetric, which implies symmetry with respect to the exchange of the two H atoms. By contrast, the A_1–B_2 couplings at the $\tilde{E}'/\tilde{D}$ and $\tilde{D}/\tilde{B}$ CIs require anti-symmetric off-diagonal terms[59,61].

To address such multi-state-coupled problems, a machine learning method with embedded physical constraints was used to construct the DPEM[59,60]. The DPEM was represented by a neural network (NN) with a 3-40-40-40-10 architecture[61,63–65]. The NN has one input layer, three hidden layers and an output layer, where the ten output nodes of the final layer correspond to the ten independent matrix elements of the DPEM: V_{11}, V_{22}, V_{33}, V_{44}, V_{12}, V_{13}, V_{14}, V_{23}, V_{24} and V_{34}. The output of one layer becomes the input for the following layer, as given by equation (3), where a is the output of one layer, b are the biases of layer m and f is the transform function of layer m:

$$n_{i,q}^{m} = \sum_{j=1}^{S^{m-1}} \left(w_{i,j}^{m} a_{j,q}^{m-1} \right) + b_i^m \, a_{i,q}^{m} = f^m \left(n_{i,q}^{m} \right). \quad (3)$$

The key ideal is that the DPEM should accurately reproduce the adiabatic energies[59,60,66]. In addition, in the proximity of a CI or AVC, the diabatic matrix elements are known a priori. For the CIs, the off-diagonal terms must vanish (by symmetry requirements) at the higher order point group (C_{2v}, $C_{\infty v}$ or $D_{\infty h}$) and the diagonal elements must match the adiabatic energies (up to reordering). For the AVC, the off-diagonal term equals half the adiabatic energy gap and the diagonal terms are given by the average of the two adiabatic energies at the configuration of the minimum energy gap[67]. To satisfy the constraints of adiabatic energy fitting and the diabatic constraints, we use the following loss function (equation (4)):

$$P = \sum_{j=1}^{N} \sum_{i=1}^{ns} w_{j,i}^{ad} \left(E_{i,j}^{fit} - E_{i,j}^{ab} \right)^2 + \sum_{j=1}^{M} \sum_{i=1}^{ns} \sum_{k=i}^{ns} s_{j,i,k}^{dia} \left(V_{j,i,k}^{fit} - V_{j,i,k}^{target} \right)^2 + 0.5t \|\mathbf{p}\|^2. \quad (4)$$

The Levenberg–Marquardt algorithm was used for optimization. N in equation (4) is the number of energy points and ns is the number of electronic states. $E_{i,j}^{fit}$ are the adiabatic energies given by diagonalizing the DEPM and the $E_{i,j}^{ab}$ are the ab initio energies. $w_{i,j}^{ad}$ are the adiabatic energy weights, dependent on energy and electronic state. M is the number of constrained matrix elements. $V_{j,i,k}^{fit}$ and $V_{j,i,k}^{target}$ are the fitted diabatic matrix elements and their corresponding target values obtained from ab initio data (explained latter). $s_{j,i,k}^{dia}$ are the switching functions for each matrix element of the DPEM, which are given as 1 if the diabatic energies are added to constrain the CI or AVC or otherwise given as zero. The last term is a regularization term, to avoid overfitting. The $\mathbf{p}$ represents all the optimized parameters (weights and biases) of the NN functions and t is a regularization parameter (set to 10^{-5}).

The following steps are used to generate the $V_{j,i,k}^{target}$ matrix elements to constrain the DPEM, which is shown in Supplementary Table 1. A characteristic factor is the multiple in each off-diagonal f_{NN} function to guarantee the correct symmetry and diabatic coupling. The rOH_1 and rOH_2 are the two OH bond lengths and θ is the bond angle (the θ and rOH_2 (inner bond) coordinates are shown in Supplementary Fig. 5).

$$\begin{aligned} V_{14} &= f_{NN} \sin\theta \, (rOH_1 - rOH_2) \quad V_{12} = f_{NN} \sin\theta \\ V_{24} &= f_{NN} \sin\theta \, (rOH_1 - rOH_2) \quad V_{13} = f_{NN} \sin\theta \\ V_{34} &= f_{NN} \sin\theta \, (rOH_1 - rOH_2) \quad V_{23} = f_{NN} \sin\theta \end{aligned} \quad (5)$$

The following three permutation invariant polynomials (PIPs) were used as the input layer of the NN:

$$\begin{aligned} pip_1 &= (rOH_1 + rOH_2)/2 \\ pip_2 &= rOH_1 rOH_2 \\ pip_3 &= rHH \end{aligned} \quad (6)$$

Electronic structure calculations were performed using MOLPRO 2015[68]. The active space contained 10 orbitals (8a′ + 2a″ in C_s symmetry) and 8 electrons. Seven electronic states of H_2O (four A′ states and three A″ states, in C_s symmetry) were calculated, using the

internally contracted multi-reference configuration interaction augmentation with the Davidson correction[69], denoted as icMRCI + Q. The correlation-consistent polarized valence quintuple-zeta (cc-pV5Z) basis set was extended to include three diffuse *s* functions, two diffuse *p* functions and three diffuse *d* functions for the O atom, while the basis set for the H atoms was cc-pV5Z plus three diffuse *s* functions and two diffuse *p* functions. The transition dipole and electronic angular momentum were also calculated at the icMRCI level.

About 8,000 points were calculated and used to fit the DPEM. The root mean square errors (RMSEs) for these adiabatic states with energy below 12 eV are 28.4 meV, 30.5 meV, 64.2 meV and 105 meV, respectively. The DPEM was validated by calculating the electronic absorption spectra of H_2O and HOD and comparing them with available experimental data for the $\tilde{B}$-$\tilde{X}$ and $\tilde{D}$-$\tilde{X}$ bands[44,45]. As Supplementary Fig. 7 shows, the agreement between experiment and current theory with regard to both the individual band profiles and the absorption cross-sections is excellent.

Quantum dynamics method

Time-dependent wavepacket simulations were performed on the constructed DPEM. The Hamiltonian, expressed in OD + H Jacobi coordinates (shown in Supplementary Fig. 10) (R, r, γ), has the following term[34,47,48,70–72]:

$$\mathbf{H} = \begin{bmatrix} \hat{T} & 0 & 0 & 0 \\ 0 & \hat{T} & 0 & 0 \\ 0 & 0 & \hat{T} & 0 \\ 0 & 0 & 0 & \hat{T} \end{bmatrix} + \begin{bmatrix} V_{11} & V_{12} & V_{13} & V_{14} \\ V_{21} & V_{22} & V_{23} & V_{24} \\ V_{31} & V_{32} & V_{33} & V_{34} \\ V_{41} & V_{42} & V_{43} & V_{44} \end{bmatrix}, \tag{7}$$

where $\hat{T}$ is the kinetic energy operator (KEO) and the $V_{nn'}$ are the DPEM elements fitted in equation (4). The KEO has the following form in atomic units:

$$\hat{T} = -\frac{1}{2\mu_R}\frac{\partial^2}{\partial R^2} - \frac{1}{2\mu_r}\frac{\partial^2}{\partial r^2} + \frac{(\hat{J}-\hat{N})^2}{2\mu_R R^2} + \frac{\hat{N}^2}{2\mu_r r^2}, \tag{8}$$

in which μ_R and μ_r are the corresponding reduced masses. $\hat{J}$ and $\hat{N}$ represent the total and diatomic rotational angular momentum operators, respectively. The electronic orbital angular momentum ($\Lambda = 1$) and spin ($s = 1/2$) of the ground state OH(OD) product are ignored in the present treatment. This approximation has been validated in previous studies; the influence of the electron orbital angular momentum can be neglected, given the magnitude of the product rotational quantum number, N[30,48].

We first transform the adiabatic dipole to a diabatic dipole (equation (9)) to handle the selection rule, using the diabatic–adiabatic transform matrix **d** obtained by diagonalizing the DPEM. Through the diabatization, the dipoles could be labelled as $\mu^d_{13}(3a_1 \to 3s)$ and $\mu^d_{12}(1b_1 \to 3p_x)$. The contribution from the $(1b_1 \to 3p_x)$ diabatic dipole is near zero, as has been noted previously[27].

$$\begin{aligned} \mu^d_{12} &= \langle \phi_{gr} | \hat{d} | \phi^d_2 \rangle = \mu^a_{12} d_{22} + \mu^a_{13} d_{23} \\ \mu^d_{13} &= \langle \phi_{gr} | \hat{d} | \phi^d_3 \rangle = \mu^a_{12} d_{32} + \mu^a_{13} d_{33} \end{aligned} \tag{9}$$

The initial wavepacket was given by the body-fixed (BF) wavefunction in the ground state multiplied by the diabatic transition dipole moments, that is,

$$\mathbf{\Psi}_0 \equiv \begin{pmatrix} 0 \\ \psi_\lambda(k=0) \\ \psi_{\lambda'}(k=0) \\ 0 \end{pmatrix} = \begin{pmatrix} 0 \\ \hat{e} \cdot \hat{u}^d_{12} \times \psi_{gr} \\ \hat{e} \cdot \hat{u}^d_{13} \times \psi_{gr} \\ 0 \end{pmatrix}. \tag{10}$$

The subscript λ denotes the electronic state. The initial wavepacket was then propagated in the Chebyshev order (k), which has the following form:

$$\mathbf{\Psi}(k) = 2D\mathrm{H}_s\mathbf{\Psi}(k-1) - D^2\mathbf{\Psi}(k-2),\ k \geq 2, \tag{11}$$

in which $\mathbf{\Psi}_1 = D\mathrm{H}_s\mathbf{\Psi}_0$ and $\mathbf{\Psi}_0$ is the initial wavepacket. Since the domain of Chebyshev polynomials is in (−1,1), the scaled Hamiltonian $\mathbf{H}_s$ is defined in (−1,1) by $\mathrm{H}_s = (\mathbf{H} - H^+\mathbf{I})/H^-$, with $H^\pm = (H_{\max} \pm H_{\min})/2$, where $H_{\max}$ and $H_{\min}$ are the upper and lower spectral bounds of the Hamiltonian, respectively. The damping function D is used to avoid unphysical reflections at the edges of the grid. The final state distribution can be calculated as follows. First, the Chebyshev correlation function $C^{Jkp}_{\lambda\upsilon N}(k)$ is calculated by projecting the wavepacket onto the rovibrational eigenfunctions of OD(X) using equation (12). $\Theta^K_N(\gamma)$ is an angular basis function dependent on γ and $\chi_{\lambda\upsilon N}(r)$ is a radial basis function dependent on r. The dot product of these two parts of the overall basis function describes one rovibrational state of OD(X).

$$C^{Jkp}_{\lambda\upsilon N}(k) = \langle \Theta^K_N(\gamma)\chi_{\lambda\upsilon N}(r) | \psi_\lambda(k) \rangle. \tag{12}$$

To monitor the accumulation of products in real time, we need to transform the wavepacket from Chebyshev order (k) to a time-dependent wavepacket and further evaluate the time-dependent correlation function through equations (13)–(15), where the J_k are Bessel functions of the first kind[73] and p is system parity.

$$\mathbf{\Psi}(t) = \sum_{k=0}^{\infty} f(k,t)\mathbf{\Psi}(k) \tag{13}$$

$$f(k,t) = (2 - \delta_{k0})e^{-iH^+t}(-i)^k J_k(tH^-) \tag{14}$$

$$C^{Jkp}_{\lambda\upsilon N}(t) = \langle \Theta^K_N(\gamma)\chi_{\lambda\upsilon N}(r) | \psi_\lambda(t) \rangle = \sum_{k=0}^{\infty} f(k,t) C^{Jkp}_{\lambda\upsilon N}(k). \tag{15}$$

We now take the half-Fourier transform of this integral over time to give an energy-dependent quantity:

$$A^{Jkp}_{\lambda\upsilon N}(E) = \frac{1}{2\pi}\int_{t=0}^{\infty} \exp(iEt) C^{Jkp}_{\lambda\upsilon N}(t). \tag{16}$$

The product can thus be tracked at different accumulated times by checking the results from different Fourier transformation steps.

$$A^{Jkp}_{\lambda\upsilon N}(E,t) = \frac{1}{2\pi}\int_{t=0}^{t} \exp(iEt) C^{Jkp}_{\lambda\upsilon N}(t). \tag{17}$$

A fundamental principle of quantum mechanics dictates that the observed energy spans a certain width at a given time, following $\Delta E = \frac{1}{t}$ in atomic units[74]. However, in the present problem, the direct dissociation dynamics exhibits similarities across a broad energy range, owing to the reflection principle[54]. Thus, we can simultaneously monitor the time evolution of the OD(X) products within an energy domain. The product distribution could be further calculated from the $A^{JK}_{\lambda\upsilon N}(E)$ or $A^{JK}_{\lambda\upsilon N}(E + \Delta E, t)$ terms via

$$T^{Jkp}_{\lambda\upsilon N}(E) = i(-1)^{K-N}\sqrt{1+\delta_{0K}}\left(\frac{\pi k_{\upsilon\lambda N}}{\mu_R}\right)^{1/2} e^{-ik_{\lambda\upsilon N}R_\infty} A^{Jkp}_{\lambda\upsilon N}(E) \tag{18}$$

$$\sigma_{\lambda\upsilon N}(E) = \frac{4\pi\omega^2}{c}\frac{1}{2J_i+1}\sum_{J=J_i-1}^{J_i+1}\sum_{K=\kappa}^{J}\frac{\delta(JJ_i1)}{3} T^{Jkp}_{\lambda\upsilon N}{}^* T^{Jkp}_{\lambda\upsilon N'}, \tag{19}$$

with the additional definitions $\kappa = \frac{1-(-1)^{J_i+p_i}}{2}$ and $k_{\lambda\upsilon N} = \sqrt{2\mu_R(E - E_{\lambda\upsilon N})}$. ω is the energy of photon and c is the speed of light. J_i is the total angular

momentum of the initial state of HOD. The anisotropy parameter β can be obtained from the T-matrix, given as

$$\bar{\sigma}_{\lambda\upsilon N}(E;\theta) = \frac{\pi\omega}{c}\frac{1}{2J_i+1}\sum_{J=J_i-1}^{J_i+1}\sum_{J'=J_i-1}^{J_i+1}\sum_{K=\lambda}^{J}\sqrt{2J+1}\sqrt{2J'+1}(-1)^{J_i+K+J+J'} \times \sum_{\kappa=0,2}(2\kappa+1)P_\kappa(\cos\theta)\begin{pmatrix} J & J' & \kappa \\ K & -K & 0\end{pmatrix}\begin{pmatrix} 1 & 1 & \kappa \\ 0 & 0 & 0\end{pmatrix}\begin{Bmatrix} 1 & 1 & \kappa \\ J & J' & J_i\end{Bmatrix} \times T^{J'Kp*}_{\lambda\upsilon N}T^{JKp}_{\lambda\upsilon N} \quad (20)$$

$$\beta_{\lambda\upsilon N} = \frac{\bar{\sigma}_{\lambda\upsilon N}(\omega;\theta)_{\kappa=2}/P_2(\cos\theta)}{\bar{\sigma}_{\lambda\upsilon N}(\omega;\theta)_{\kappa=0}}. \quad (21)$$

θ is the angle between the fragment recoil direction and the light polarization direction, and $P_k(\cos\theta)$ is a Legendre polynomial.

The scattering wavefunction is calculated via

$$\mathbf{\Psi}(E) = \sum_{k=0}^{\infty} c(k,E)\mathbf{\Psi}(k) \quad (22)$$

$$c(k,E) = (2-\delta_{k0})\exp(-ik\arccos E_s). \quad (23)$$

Projection of the total wavefunction onto the OD(X, υ) manifold is obtained by integrating over the internuclear distance:

$$\psi_{\lambda,\upsilon}(R,\gamma) = \int \chi^*_{\lambda,\upsilon,N}(r)\psi_\lambda(R,r,\gamma)\mathrm{d}r. \quad (24)$$

In addition, similar to the time-dependent products, the wavefunction can be examined at different Fourier transformation steps to obtain the time-dependent scattering wavefunction for a specific energy[72].

To decompose the T-matrix, the direct and indirect pathway contributions were calculated by evaluating the integral in equation (17) from $t = 0$ to a dividing time and from the dividing time to infinity, respectively. The interference term was then obtained as the difference between the square of the total T-matrix and the sum of the squares of these direct and indirect components.

Surface hopping calculations

The calculations used the fewest switches with time uncertainty method (FSTU), implemented in the ANT programme[75]. The trajectories were propagated in the adiabatic representation, with transitions using the stochastic decoherence scheme incorporating FSTU. The initial conditions for each trajectory were sampled from the ground-state Wigner distribution of HOD, with propagation starting on the $\tilde{D}$ state PES. The total energy was fixed at 10.76 eV, which corresponds to an excitation energy around 10.26 eV. The trajectory was terminated once either the OD or OH bond length exceeded 10 Bohr. A total of 4.8 million trajectories were simulated.

Data availability

The data supporting the findings of this study can be accessed via figshare at https://doi.org/10.6084/m9.figshare.30883529 (ref. 76). Source data are provided with this paper.

Code availability

Fortran code used for the present work is available via GitHub at https://github.com/Shanyu-keyboard-geochemist/Photodissociation-code/tree/main.

References

57. An, F. et al. Adiabatic potential energy surfaces and photodissociation mechanisms for highly excited states of H_2O. *Chin. J. Chem. Phys.* **35**, 104–116 (2022).
58. Hirst, D. M. & Child, M. S. Ab initio bending potential-energy curves for Rydberg states of H_2O. *Mol. Phys.* **77**, 463–476 (1992).
59. Hou, S., Wang, Z. & Xie, C. Accurate and efficient schemes for mapping out two isolated seams of conical intersections with neural networks solely based on adiabatic energies: a case study of $H^+ + NO(X\,^2\Pi) \rightarrow H + NO^+(X\,^1\Sigma)$. *J. Phys. Chem. A* **128**, 7046–7054 (2024).
60. Li, C., Hou, S. & Xie, C. Constructing diabatic potential energy matrices with neural networks based on adiabatic energies and physical considerations: toward quantum dynamic accuracy. *J. Chem. Theory Comput.* **19**, 3063–3079 (2023).
61. Guan, Y., Xie, C., Yarkony, D. R. & Guo, H. High-fidelity first principles nonadiabaticity: diabatization, analytic representation of global diabatic potential energy matrices, and quantum dynamics. *Phys. Chem. Chem. Phys.* **23**, 24962–24983 (2021).
62. Guan, Y., Yarkony, D. R. & Zhang, D. Permutation invariant polynomial neural network based diabatic ansatz for the (E + A) × (e + a) Jahn-Teller and Pseudo-Jahn-Teller systems. *J. Chem. Phys.* **157**, 014110 (2022).
63. Guan, Y., Xie, C., Guo, H. & Yarkony, D. R. Toward a unified analytical description of internal conversion and intersystem crossing in the photodissociation of thioformaldehyde. I. Diabatic singlet states. *J. Chem. Theory Comput.* **19**, 6414–6424 (2023).
64. Guan, Y., Zhang, D., Guo, H. & Yarkony, D. R. Representation of coupled adiabatic potential energy surfaces using neural network based quasi-diabatic Hamiltonians: 1,2 ^{2}A′ states of LiFH. *Phys. Chem. Chem. Phys.* **21**, 14205–14213 (2019).
65. Guan, Y., Xie, C., Guo, H. & Yarkony, D. R. Enabling a unified description of both internal conversion and intersystem crossing in formaldehyde: a global coupled quasi-diabatic Hamiltonian for its S_0, S_1, and T_1 states. *J. Chem. Theory Comput.* **17**, 4157–4168 (2021).
66. Guan, Y., Chen, Q. & Varandas, A. J. C. Accurate diabatization based on combined-hyperbolic-inverse-power-representation: 1,2 ^{2}A′ states of BeH_2^+. *J. Chem. Phys.* **160**, 154105 (2024).
67. Jasper, A. W., Hack, M. D., Truhlar, D. G. & Piecuch, P. Coupled quasidiabatic potential energy surfaces for LiFH. *J. Chem. Phys.* **116**, 8353–8366 (2002).
68. Werner, H. J. et al. Molpro: a general-purpose quantum chemistry program package. *Wiley Interdiscip. Rev. Comput. Mol. Sci.* **2**, 242–253 (2012).
69. Knowles, P. J. & Werner, H.-J. An efficient method for the evaluation of coupling coefficients in configuration interaction calculations. *Chem. Phys. Lett.* **145**, 514–522 (1988).
70. Hu, X., Zhou, L. & Xie, D. State-to-state photodissociation dynamics of the water molecule. *WIREs Comput. Mol. Sci.* **8**, e1350 (2018).
71. Zhou, L., Lin, G. S. & Xie, D. State to state photodissociation dynamics of D_2O in the *B* band. *J. Chem. Phys.* **139**, 114303 (2013).
72. Zhou, L., Jiang, B., Xie, D. & Guo, H. State-to-state photodissociation dynamics of H_2O in the *B* band: competition between two coexisting nonadiabatic pathways. *J. Phys. Chem. A* **117**, 6940–6947 (2013).
73. Roncero, O. & del Mazo-Sevillano, P. MADWAVE3: a quantum time dependent wave packet code for nonadiabatic state-to-state reaction dynamics of triatomic systems. *Comput. Phys. Commun.* **308**, 109471 (2025).
74. Landau, L. D. & Lifshitz, E. M. *Quantum Mechanics: Non-relativistic Theory* Vol. 3 (Elsevier, 2013).
75. Shu, Y., Zhang, L. & Truhlar, D. G. ANT 2023: a program for adiabatic and nonadiabatic trajectories. *Comput. Phys. Commun.* **296**, 109021 (2024).
76. Han, S. Data for the figures. *figshare* https://doi.org/10.6084/m9.figshare.30883529 (2025).

Acknowledgements

We thank C. Xie for the suggestion on diabatization and Y. Guan for providing Fortran code for training neural network, S. Su for helping data acquisition, the staff members of the Molecular Photochemistry System (31127.02.DCLS.CESMP) at the Dalian Coherent Light Source (31127.02.DCLS) for providing technical support and assistance in data collection, and M. Ashfold (University of Bristol) for helpful feedback on earlier drafts of this paper. This work was supported by the Strategic Priority Research Program of the Chinese Academy of Sciences (grant numbers XDB0970000 and XDB0970200), the Quantum Science and Technology-National Science and Technology Major Project (2021ZD0303304 and 2021ZD0303305), the National Natural Science Foundation of China (grant numbers 22241304 and 22225303), and the National Natural Science Foundation of China (NSFC Center for Chemical Dynamics (grant number 22288201)). The theoretical work was supported by the National Natural Science Foundation of China (grant numbers 42494854, 22473057, 22233003 and 22241302). X.Y. thanks the Guangdong Science and Technology Program (grant numbers 2019ZT08L455 and 2019JC01X091) and the Shenzhen Science and Technology Program (grant number ZDSYS20200421111001787). All calculations were performed in the High-Performance Computing Center (HPCC) at Nanjing University.

Author contributions

K.Y. and X.Y. designed the experiments. Z. Luo and Z. Li performed the experiments. Z. Luo and K.Y. analysed the data. J.W., L.Z., X.H. and S.H. performed the theoretical calculations. J.W., X.H., S.H., D.X. and H.G. analysed the results. J.W., S.H., Z. Luo, H.G. and K.Y. prepared the paper.

Competing interests

The authors declare no competing interests.

Additional information

Supplementary information The online version contains supplementary material available at https://doi.org/10.1038/s41557-026-02078-w.

Correspondence and requests for materials should be addressed to Shanyu Han, Daiqian Xie or Kaijun Yuan.

Peer review information *Nature Chemistry* thanks Graham Worth and the other, anonymous, reviewer(s) for their contribution to the peer review of this work. Peer reviewer reports are available.